

Telling different unravelings apart via nonlinear quantum-trajectory averages

Eloy Piñol,^{1,*} Th. K. Mavrogordatos,^{1,*} Dustin Keys,² Romain Veyron,¹ Piotr Sierant,¹ Miguel Angel García-March,³ Samuele Grandi,¹ Morgan W. Mitchell,^{1,4} Jan Wehr,² and Maciej Lewenstein^{1,4,†}

¹*ICFO – Institut de Ciències Fotòniques, The Barcelona Institute of Science and Technology, 08860 Castelldefels (Barcelona), Spain*

²*Department of Mathematics, The University of Arizona Tucson, AZ 85721-0089 USA*

³*Instituto Universitario de Matemática Pura y Aplicada,*

Universitat Politècnica de València, Camino de Vera, s/n, 46022 Valencia, Spain

⁴*ICREA – Institució Catalana de Recerca i Estudis Avançats, 08010 Barcelona, Spain*

(Dated: July 19, 2024)

The Gorini-Kossakowski-Sudarshan-Lindblad master equation (ME) governs the density matrix of open quantum systems (OQSs). When an OQS is subjected to weak continuous measurement, its state evolves as a stochastic quantum trajectory, whose statistical average solves the ME. The ensemble of such trajectories is termed an unraveling of the ME. We propose a method to operationally distinguish unravelings produced by the same ME in different measurement scenarios, using nonlinear averages of observables over trajectories. We apply the method to the paradigmatic quantum nonlinear system of resonance fluorescence in a two-level atom. We compare the Poisson-type unraveling, induced by direct detection of photons scattered from the two-level emitter, and the Wiener-type unraveling, induced by phase-sensitive detection of the emitted field. We show that a quantum-trajectory-averaged variance is able to distinguish these measurement scenarios. We evaluate the performance of the method, which can be readily extended to more complex OQSs, under a range of realistic experimental conditions.

PACS numbers: 32.50.+d, 42.50.Ar, 42.50.-p

Keywords: Quantum trajectories, Poisson process, Wiener process, Dyson expansion, homodyne and heterodyne detection, direct photoelectron counting, detector efficiency

Introduction.—Quantum systems interacting with Markovian environments are ubiquitous in the physical sciences. A main tool for studying their dynamics is the deterministic Gorini-Kossakowski-Sudarshan-Lindblad (GKSL) master equation (ME) [1, 2]. This specifies the time evolution of the density matrix $\rho(t)$ as the system experiences both coherent and incoherent processes, with the latter involving leakage of state information to the environment [3–6]. Despite its generality and wide use, the GKSL ME does not fully describe the quantum dynamics when the environment includes measurement devices, which convert a portion of the leaked information to usable form. The temporal evolution conditioned on the measurement record m defines a *quantum trajectory*, in the ideal case expressed as the pure state $\rho_m(t) = |\psi_m(t)\rangle\langle\psi_m(t)|$. The unraveling into pure states can be performed whenever the continuous evolution in the GKSL ME is governed by a commutator with a non-Hermitian Hamiltonian, and the initial state is pure. The resulting nonlinear Schrödinger equation governing the evolution of normalized states in quantum-trajectory theory is a straightforward consequence of conditioning and is not considered to arise from any previously unknown inherent stochasticity [7]. Averaging $\rho_m(t)$ over the measurement record solves the GKSL ME [8]. The identification of the $\rho(t)$ with the ensemble average of $\rho_m(t)$ is

an example of an *unraveling* of the ME into a stochastic equation for the pure state $\rho_m(t)$ [9–18]. Evidently, different measurement schemes correspond to different unravelings and lead to different ensembles of quantum trajectories. Unravelings thus provide information that is not available from the corresponding ME.

Quantities that are linear in the density matrix $\rho(t)$, such as averages of observables, are fully determined by the GKSL ME and, therefore, are independent of the choice of the unraveling dictated by a given measurement scheme. In this Letter, we develop nonlinear measures to differentiate unravelings, thus opening a way to access the physics beyond the ME. We demonstrate that evaluating an expectation value of a physical observable for a specified quantum trajectory $\rho_m(t)$, performing a nonlinear operation on the obtained result, and averaging the result over the measurement record, yields a quantity that allows for distinguishing different unravelings of the same GKSL ME. We focus on a paradigmatic open quantum system, the resonance fluorescence of a two-level atom, and consider unravelings corresponding to direct photodetection and to homodyne/heterodyne detection. We remark that while direct photodetection enjoys an obvious link with intensity correlations, measuring the spectrum of squeezing is inherently tied with homodyne detection, which provides a phase reference to a phase-dependent phenomenon [7].

The unravelings.—Electron shelving [19, 20] paved the way to the first observations of quantum jumps [21–23], followed by several atomic [24–26] and solid-state physics experiments [27–29]. The theoretical description

* These two authors contributed equally

† maciej.lewenstein@icfo.es

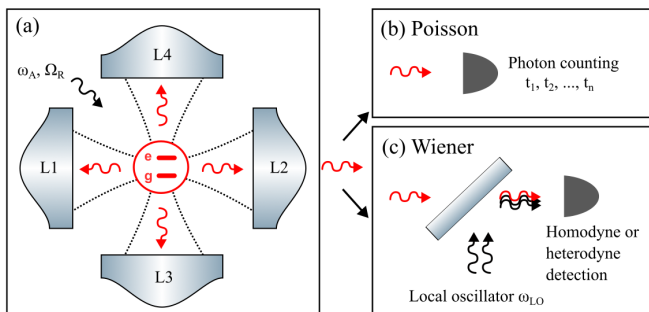


FIG. 1. *Schematic representation of the two main unraveling schemes.* In this setup, the trapped two-state atom is illuminated in a Maltese-cross arrangement [57, 58] shown in (a). The output radiation escaping a particular lens is directed to either: (b) a collection of avalanche photodiodes (APDs) producing a time-series of “click” events (Poisson-type unraveling); (c) a mixer with a strong local oscillator field, to substantiate either a homodyne ($\omega_{LO} = \omega_A$) or a heterodyne measurement ($|\omega_{LO} - \omega_A| \gg \gamma$) scheme (Wiener-type unraveling).

of these investigations dates back to early works [30–39] that stimulated the development of quantum trajectory theory [10, 40–47]. Two unravelings of the GKSL ME that play a fundamental role in the understanding of the quantum trajectories are: (i) Poisson unraveling, related to direct photodetection and the so called quantum Monte Carlo wave function approach [12, 48–51]; and (ii) Wiener-type unraveling (the quantum state diffusion model proposed by Gisin and Percival) [52, 53], relating conditional quantum dynamics to a continuous Wiener process [54]. In the context of atomic physics experiments, the distinct unravelings correspond to different photodetection schemes [5], see Fig. 1. The Poisson unraveling is relevant for the direct photodetection experiments, while the continuous Wiener process arises in homodyne and heterodyne photodetection schemes [10, 55].

The disparities between the experimental setups is reflected in the different nature of quantum trajectories [53]. The Wiener process yields a continuous evolution of the system state $|\psi(t)\rangle$. In contrast, the acts of direct photodetection at times $t_1 < t_2 < \dots < t_n$ collapse the conditional wavefunction. The resulting time evolution of $|\psi(t)\rangle$ is discontinuous and the final state at $t > t_n$ depends, in general, on a particular sequence of emission times $|\psi(t)\rangle = |\psi_{t_1, \dots, t_n}(t)\rangle$. By collecting photon counting records, the experimenter effectively determines the quantum trajectory of the atom. The entanglement between the electromagnetic field and the atom is the key ingredient that allows for the inference of the atom’s state based on the photodetection events [53, 56]. In particular, Nha and Carmichael demonstrated that the degree of entanglement depends on how information in the environment is read [56].

Source Master Equation and linear averages.—Our starting point is the GKSL ME of resonance fluorescence, governing the unconditional evolution of the reduced sys-

tem density matrix ρ ,

$$\begin{aligned} \frac{d\rho}{dt} = \mathcal{L}\rho = & -i\frac{1}{2}\omega_A[\sigma_z, \rho] - i\Omega[e^{-i\omega_A t}\sigma_+ + e^{i\omega_A t}\sigma_-, \rho] \\ & + \frac{\gamma}{2}(2\sigma_-\rho\sigma_+ - \sigma_+\sigma_-\rho - \rho\sigma_+\sigma_-), \end{aligned} \quad (1)$$

where we have neglected thermal excitation [59]. In the ME (1), $\sigma_+, \sigma_-, \sigma_z$ are the raising, lowering and inversion operators (represented by Pauli matrices), respectively, for the two-level atom coherently driven by a resonant laser field of frequency ω_A ; $\Omega_R = 2\Omega$ is the Rabi frequency at which the two-state atom periodically oscillates between its ground and excited states, and γ is the spontaneous emission rate. The solution of the corresponding optical Bloch equations yields the following expression for the average inversion when the atom is initialized in its ground state,

$$\overline{\langle\sigma_z(t)\rangle} = S_z \left[1 + Y^2 e^{-(3\gamma/4)t} \left(\cosh \delta t + \frac{(3\gamma/4)}{\delta} \sinh \delta t \right) \right], \quad (2)$$

where $Y \equiv \sqrt{2}\Omega_R/\gamma$, $\delta \equiv \frac{\gamma}{4}\sqrt{1 - 8Y^2}$ and $S_z = -1/(1 + Y^2)$ is the steady-state inversion. Hereinafter, we denote by $\langle\cdot\rangle$ the quantum mechanical average over an individual realization. For strong driving ($Y \gg 1$) the average inversion exhibits damped oscillations at Ω_R , relaxing to $0 + \mathcal{O}(\gamma^2/\Omega^2)$. Equation (2) is an example of a typical linear average computed directly from the ME, against which our nonlinear averages are to be compared. We now describe the nonlinear averages.

Nonlinear averages beyond the density-matrix formalism.—The idea underlying our approach is to perform a nonlinear operation on a quantum mechanical expectation value evaluated for an *individual* quantum trajectory prior to averaging of the result over the ensemble of quantum trajectories denoted by $\langle\cdot\rangle$. A characteristic nonlinear average of our focus is the quantity $\text{Var}(\sigma_z) \equiv \overline{\langle\sigma_z(t)\rangle^2} - [\overline{\langle\sigma_z(t)\rangle}]^2$, which we hereinafter call *quantum-trajectory-averaged variance* (QTAV).

The results depicted in Fig. 2 substantiate the pivotal influence of the environment when collecting records of a strongly driven two-state atom and taking a sum over a collection of them. The two principal unravelings are presented in their ability to produce an ostensibly disparate $\text{Var}(\sigma_z)$, while the corresponding average inversion remains unchanged. For the direct photodetection [60–62], corresponding to the Poisson-type unraveling of the ME, we obtain an exact expression for $\text{Var}(\sigma_z)$ based on the waiting-time distribution [63]. For $\gamma t \gg 1$, the asymptotic expression for the variance, including first-order terms in γ/Ω of different frequencies, reads [59]

$$\begin{aligned} \text{Var}(\sigma_z) = & \frac{1}{2} \left\{ 1 + e^{-\gamma t/2} \cos(4\Omega t) + \frac{\gamma}{8\Omega} e^{-\gamma t/2} [4 \sin(4\Omega t) \right. \\ & \left. - \sin(6\Omega t) - 3 \sin(2\Omega t)] + \mathcal{O}(\gamma^2/\Omega^2) \right\}. \end{aligned} \quad (3)$$

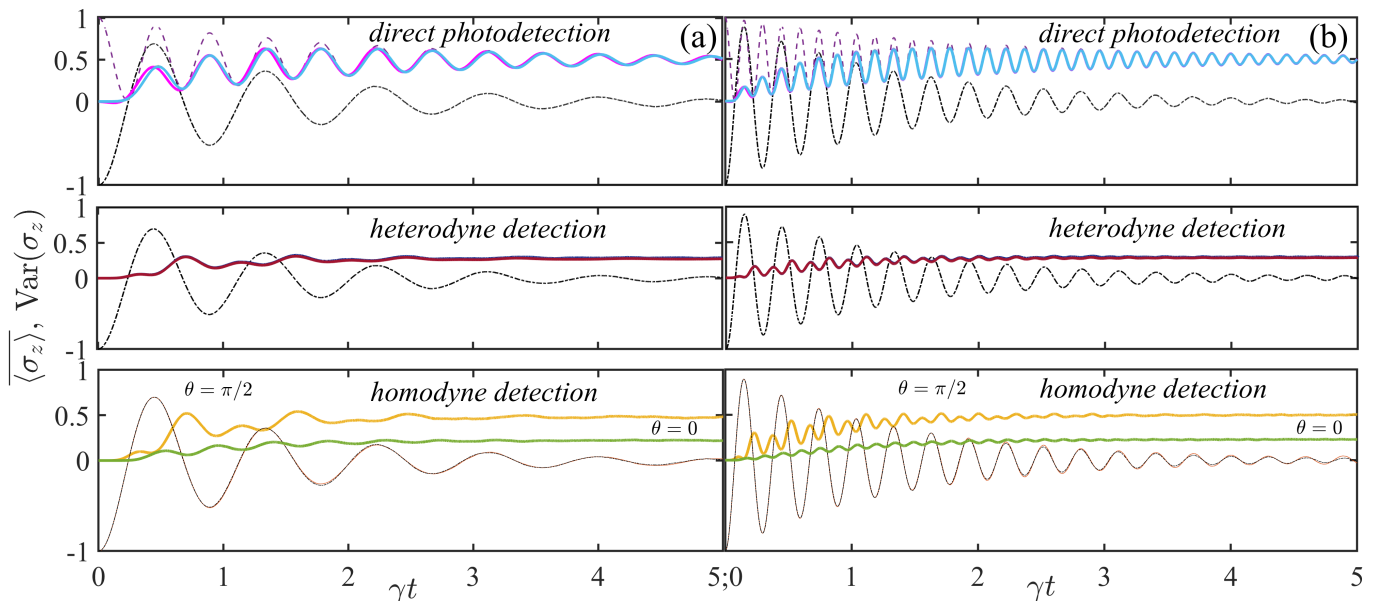


FIG. 2. *Linear vs. nonlinear quantum-trajectory averages for three principal unravelings.* Monte-Carlo averages over 10^4 realizations of the QTAV $\text{Var}(\sigma_z)$ plotted against the dimensionless time γt for a Poisson-type unraveling (direct photodetection) and two Wiener-type unravelings (homodyne and heterodyne detection) as indicated in each panel, for (a) $Y = 10$ and (b) $Y = 30$, with the two-level atom initialized in its ground state. The oscillatory dot-dashed curves with alternating sign in all frames depict the average inversion $\langle \sigma_z(t) \rangle$. In the uppermost panels of both frames, the pink and blue curves depict $\text{Var}(\sigma_z)$ obtained from the perturbative treatment of the Dyson-series expansion to first order in γ/Ω , and the moment-based equations, respectively. The latter results are indistinguishable from the Monte-Carlo simulations on the scale of the figure. The dashed curves (in purple) depict the asymptotic expression (3). For heterodyne detection, the QTAV obtained from the numerical simulations (in blue) is indistinguishable from the moment-based method results (in red). Homodyne detection is performed with the local-oscillator phase selected along the anti-squeezed and squeezed quadratures of the fluorescent field, at $\theta = 0$ and $\pi/2$, respectively, corresponding to the same inversion average (brown curve overlapping with the dot-dashed).

The first observation to be made from Eq. (3) is that the amplitude of the dominant term (second term in the sum) to the QTAV – revealing a frequency doubling with respect to the inversion – is independent of Ω . The variance ultimately relaxes to $1/2$, as we can see in both uppermost panels of frames (a) and (b). The asymptotic evolution to the steady state is in very good agreement with the exact Monte-Carlo simulations as well as with the perturbative treatment of the Dyson-series expansion for the variance [59], and the truncated hierarchy of moments produced from the adjoint Lindbladian.

The time evolution of the QTAV is significantly altered, see the middle panels of Fig. 2, when one places a beam splitter and a local oscillator in the environment, and the fluorescent signal interferes with the latter before photodetection [Fig. 1(c)], corresponding to the heterodyne detection and exemplifying Wiener-type unraveling. The frequency doubling is also in evidence although the contrast in the oscillations is visibly suppressed. The light scattered by the two-level emitter is squeezed in the field quadrature that is in phase with the mean scattered field amplitude $\propto \langle \sigma_-(t) \rangle$ [64, 65]. The bottom panel in each frame shows that the QTAV responds differently to the detection of the squeezed *vs.* the direction of the anti-squeezed quadrature of the fluorescent field, *i.e.*, along an axis perpendicular to the equator of the Bloch sphere

where quantum fluctuations are redistributed among the quadratures.

Ensemble moments and adjoint Lindbladian.—To provide some analytical grounding to the behavior of the QTAV, we will delineate a method akin to the optical Bloch equations extended to account for the nonlinear averages. The contributions from the Itô corrections to the ensemble moments can be found easily in the Heisenberg picture [66]. Under the Poisson unraveling for an observable A [41] (we denote $\langle A(t) \rangle$ by $\langle A \rangle_t$):

$$d\langle A \rangle_t = \langle \mathcal{L}^\dagger[A] \rangle_t dt + \left(\frac{\langle \sigma_+ A \sigma_- \rangle_{t-} - \langle A \rangle_{t-}}{\langle \sigma_+ \sigma_- \rangle_{t-}} \right) d\tilde{N}(t), \quad (4)$$

where \tilde{N} is the compensated Poisson process, $d\tilde{N} = dN - \gamma \langle \sigma_+ \sigma_- \rangle_t dt$, with a future pointing differential of expected value zero. This means that the ensemble average, here denoted by \mathbb{E} for readability, is just

$$d\mathbb{E} \langle A \rangle_t = \mathbb{E} \langle \mathcal{L}^\dagger[A] \rangle_t dt,$$

which is the Heisenberg unraveling of the ME. It is useful to consider this equation for a Hilbert-Schmidt basis X_i for the space of observables. Call the quantum expectation $x_i = \langle X_i \rangle$. Thus each observable A has a corresponding vector a such that $\langle A \rangle = (a, x)$. If we

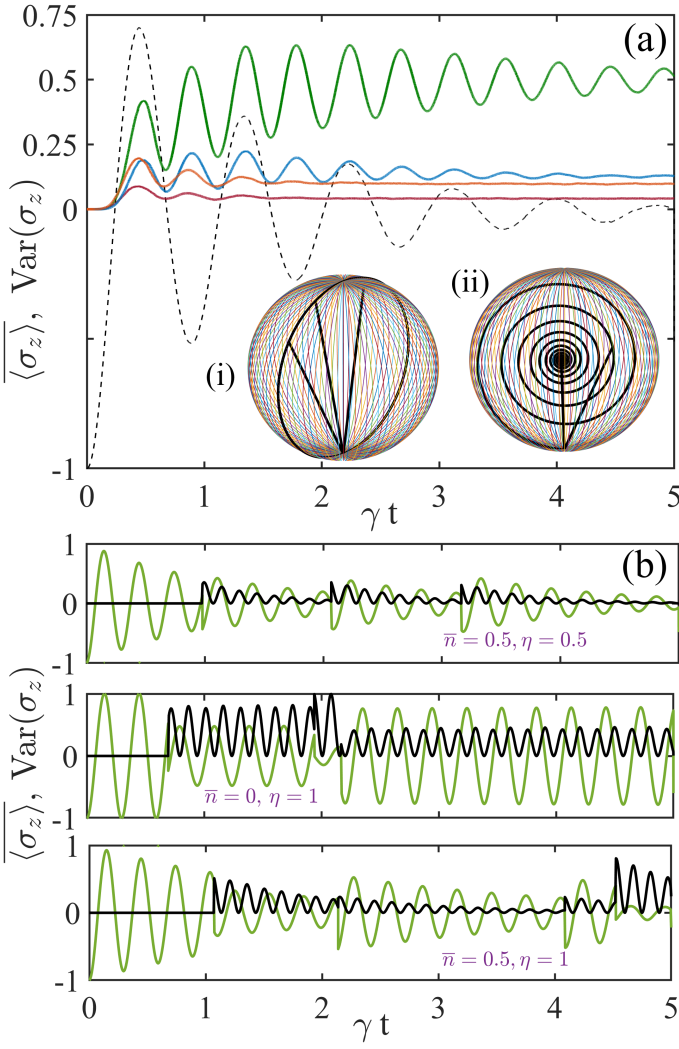


FIG. 3. *Experimental limitations and decay of “conditional” coherence.* (a) Monte-Carlo average over 10^4 realizations of the QTA V $\text{Var}(\sigma_z)$ obtained with $Y = 10$, plotted against the dimensionless time γt for the ideal case $\bar{n} = 0, \eta = 1$ (in green), $\bar{n} = 0, \eta = 0.5$ (in blue), $\bar{n} = 1, \eta = 1$ (in orange), and $\bar{n} = 1, \eta = 0.5$ (in red). The dashed curve depicts $\overline{\langle \sigma_z(t) \rangle}$ in the ideal case. The inset shows two sample trajectories in the Bloch sphere obtained with $Y = 30$ and for $\bar{n} = 0, \eta = 1$ (i) and $\bar{n} = 1, \eta = 0.8$ (ii). (b) Monte-Carlo average over *two* realizations for the atomic inversion, $\overline{\langle \sigma_z(t) \rangle}$ (in green) and $\text{Var}(\sigma_z)$ (in black) for the values of \bar{n}, η indicated in each textbox.

use the basis corresponding to the three Pauli matrices and the identity, all normalized in the Hilbert-Schmidt norm, then the vector for $A = \sigma_z$ is $a = (0, 0, 0, \sqrt{2})$. Since a is just a constant vector, generally we have that $\mathbb{E} \langle A \rangle = \mathbb{E}(a, x) = (a, \mathbb{E}x)$ and the square of the quantum expectation becomes $\langle A \rangle^2 = \sum_{ij} a_i a_j x_i x_j$ so that $\mathbb{E} \langle A \rangle^2 = \sum_{ij} a_i a_j \mathbb{E} x_i x_j$ and so to see how the ensemble average of square of the quantum expectation evolves in time it is necessary to know how $\mathbb{E} x_i x_j$ evolves. In the

Poisson case, we obtain

$$\begin{aligned} d\mathbb{E} x_i x_j &= \mathbb{E} \left(x_i \langle \mathcal{L}^\dagger[X_j] \rangle_t dt + \langle \mathcal{L}^\dagger[X_i] \rangle_t x_j dt \right) + \\ &\mathbb{E} \left(\frac{\langle \sigma_+ X_i \sigma_- \rangle_t}{\langle \sigma_+ \sigma_- \rangle_t} - x_i \right) \left(\frac{\langle \sigma_+ X_j \sigma_- \rangle_t}{\langle \sigma_+ \sigma_- \rangle_t} - x_j \right) \\ &\times \langle \sigma_+ \sigma_- \rangle_t dt = \mathbb{E} \left(x_i (u^j, x) + (u^i, x) x_j \right. \\ &\left. + \frac{1}{(l, x)} ((v^i, x_i) - x_i(l, x)) ((v^j, x) - x_j(l, x)) \right) dt, \end{aligned}$$

using the fact that $d\tilde{N}d\tilde{N} = dN$ with the rate of the Poisson process being $\gamma \langle \sigma_+ \sigma_- \rangle_t dt$ and in the last line using u^j as the vector corresponding to $\mathcal{L}^\dagger[X_j]$, l as $\sigma_+ \sigma_-$, and v^j as $\sigma_+ X_j \sigma_-$. This is an ordinary differential equation which however does not close since it requires higher order moments such as $\mathbb{E} x_i x_j x_k$. Again, using the Itô product rule we can calculate the equation for the higher order moments to obtain a system of ordinary differential equations which still do not close. We can repeat this procedure to arbitrarily high order but at some point we have to truncate. It can be shown that this truncation is linear in the moments, which allows us to solve the system using traditional methods of solving linear systems of ODEs. The Wiener case [41, 52] can be similarly approximately solved by using the Heisenberg equation [66]

$$d \langle A \rangle_t = \langle \mathcal{L}^\dagger[A] \rangle_t dt + \left(\sqrt{\gamma} \langle A(\sigma_- - \langle \sigma_- \rangle_t) \rangle \frac{dW(t)}{\sqrt{2}} + \text{h.c.} \right),$$

where W is a complex Wiener process. Solutions to these kind of truncated systems of equations for the two principal unravelings are depicted in Fig. 2, in very good agreement with the Dyson-expansion method and Monte-Carlo averages.

Direct photodetection revisited and compromised.— Having laid out an operational approach to distinguish the different unravelings, let us return to direct photodetection and discuss the most commonly encountered limitations in an actual experiment, where the density matrix *cannot* be unraveled into a pure-state ensemble, in which we would have a conditional wavefunction obeying a Schrödinger equation with a non-Hermitian Hamiltonian. This happens for a limited detector efficiency $\eta < 1$ and/or a surrounding bath with appreciable thermal excitation \bar{n} [59].

Figure 3 testifies to the rapid degradation of $\text{Var}(\sigma_z)$ as we move away from a pure-state description of the conditional dynamics. The QTA V responds to quantum jumps taking place in the course of individual realizations. This is evident from Fig. 3(b) where $\text{Var}(\sigma_z)$ remains zero until a spontaneous-emission event occurs in a pair of realizations. For an imperfect detector or for a thermally excited bath, the regression of fluctuations following a jump is damped. The decay concerns the coherent part of the evolution between spontaneous emissions, at a rate much faster than γ , for typical experimental parameters where $\eta \ll 1$. The inset of Fig. 3(a) shows how sample trajectories spiral towards the center of the Bloch sphere,

while individual jumps reset the evolution to the south pole.

Since the intensity correlation of the scattered light reflects a nonexclusive probability of photocounting coincidences, the limited detector efficiency can be counterbalanced by increasing the number of photon “clicks” N in the course of a long experimental run. Indeed, for the setup pictured in Fig. 1(a), we have concluded that the signal-to-noise ratio for $g^{(2)}(\gamma\tau \gg 1)$ in a window about one inverse of the coherence time scales with \sqrt{N} [59]. This allows the determination of $\text{Var}(\sigma_z)$ from single realizations as low as 10^{-3} , the order of magnitude Monte-Carlo simulations indicate for $\eta \lesssim 0.05$. This order of magnitude can be increased using high numerical aperture collection systems [57, 67] and efficient single-photon detectors [68].

Conclusions and outlook.—In summary, we have expanded upon the fundamental concept of the variance in quantum mechanics going beyond the conventional density-matrix formulation. The different environments devised to collect the output of an open quantum system show up in a markedly different response of a quantity where nonlinear operations are performed to *individual* realizations prior to averaging over their ensemble. This is in contrast to linear observable averages where the complementary measurement strategies all abide by the predictions of the GKSL equation, and multi-time correlations – such as the intensity correlation function – are obtained via the quantum regression formula. Following our strategy, we need to set the initial point for two copies of the system (here a ground-state reset for direct photodetection) and then post-select the trajectories in such a way that the photocounting record is the

same with satisfactory accuracy. *Ergo*, one gains, in principle, the ability to characterize the experiment’s power to collapse the wavefunction and add information to the memory carried by a state conditioned on all events that have taken place along a single trajectory.

This ability allows for an experimentally oriented test of the objective quantum state assumption via an EPR steering inequality [69, 70]; direct photodetection has been argued to be ‘more quantum’ than its Wiener-type counterparts [69–71]. While we have focused on two primary unravelings, the possibilities are in fact endless as different output channels open up. For example, Barchielli and Gregoratti have used a measurement-based feedback protocol to assess the non-Markovian evolution of a coherently driven and continuously monitored two-level atom. The included delay has experimental consequences, modifying the Mandel Q parameter alongside the spectrum of the emitted light [72]. In general, non-Markov open systems cannot be given a trajectory interpretation built around measured outputs, as measuring non-Markov environments interferes with the reduced system dynamics. One sub-class of trivially non-Markov open systems has been recently approached using trajectories [73]. It would be interesting to extend our considerations to non-Markovian evolution case [72]. Finally, our conclusions are reflected by recent investigations of quantum many-body systems studied in the context of quantum computing and quantum simulation [74–76]. Quantum trajectories arising due to multiple measurements of the system’s state, when analyzed by relevant (nonlinear) statistical measures such as entanglement entropy, exhibit phase transitions [77–84], that are not evident in the average state [85–88] unless specifically tuned feedback mechanisms are employed [89–96].

SUPPLEMENTARY INFORMATION

In the supplementary material, we first detail the calculation of the quantum-trajectory-averaged variance $\text{Var}(\sigma_z)$ for the Poisson-type unraveling, via the Dyson-series expansion of the conditional reduced system density operator. We derive exact and approximate results, the latter in the limits of strong and weak driving where asymptotic expressions can be obtained. Secondly, we expand on the generality of the moment-based method applicable to the two principal types of unraveling (Poisson and Wiener). We also connect the quadrature amplitude squeezing encountered in resonance fluorescence to $\text{Var}(\sigma_z)$. Finally, we take into account experimental imperfections and discuss a strategy to determine nonlinear averages in an exemplary and pioneering system of a single trapped fluorescing ^{87}Rb atom whose output radiation is collected by four partially transmitting mirrors in a Maltese-cross arrangement.

1. Introduction: record making and complementarity

The theory of quantum trajectories ultimately attempts to describe the energy exchange between light and atoms, given both the quantum and wave aspects of light. The exchange must be described in a background where the quantum indicates discontinuity while the wave indicates continuity, and quantum trajectories fit both aspects in an evolution over time [9]. They employ the random stochastic processes and a formal generalization of the quantum jump to account for coherence [10, 39]. Both event-enhanced quantum theory [14] and consistent histories [13] emphasize the need to attach meaningful time series of real numbers to a quantum evolution. The series are the records obtained in the scattering scenario of a quantum optical experiment.

By producing photon counting records, we effectively define the environment by a particular idealization of what

might lie in the path of the scattered field – a perfectly absorbing boundary. Every photon scattered by the two-state atom is then used up making a record appropriate to this environment. Other idealized environments will produce different records, and disentangle the system and environment in different ways [56]. There are many different environments that might, in fact, be encountered by the scattered field, all consistent with the master equation (ME). Different environments correspond to mutually exclusive methods of record making, since every photon produces one and only one happening. Each idealized environment defines a self-consistent pure-state unraveling. This is how quantum-trajectory theory encounters Bohr’s complementarity. Apart from direct photodetection, there is another particularly important way of making records. It introduces a beam splitter and a local oscillator into the environment, and after the beam splitter every photon is counted. The scheme of homodyne and heterodyne detection uses *interference* to unveil aspects of the scattering process associated with a wave amplitude and a spectrum [53]. In the sections that follow, we will visit these complementary unravelings of the ME of resonance fluorescence, when producing the single realizations which make the quantum-trajectory-averaged variance (QTAV).

2. Resonance fluorescence and waiting-time distribution

We work with the paradigmatic system of resonance fluorescence, comprising a coherently driven two level atom (whose ground and excited states are denoted by $|\downarrow\rangle$ and $|\uparrow\rangle$, respectively) immersed in the vacuum reservoir. The derivation of the photoelectron counting distribution by Mollow [60] and Cook [61, 62] is based on a hierarchy of equations that yield the probabilities for finding n photons in the multimode fluorescent field. These equations were then used in the analysis of quantum jumps [50].

In such a system, the trajectories themselves are Markovian (as well as the averaged dynamics conforming to the Gorini-Kossakowski-Sudarshan-Lindblad (GKSL) equation), since the dynamical evolution is reset to the same state following a quantum jump. As usual, we denote by σ_- and σ_+ the lowering and raising system operators, respectively, Ω is the Rabi frequency which is taken real without loss of generality, and γ is the spontaneous decay rate. The conditional evolution of the system state under direct photodetection (with unit detector efficiency) is described by the ME [1, 2]

$$\dot{\rho}_c = \mathcal{L}\rho_c = (\ell + J)\rho_c, \quad (\text{S.1})$$

where in the interaction picture we may write

$$\ell\rho_c = [1/(i\hbar)][H, \rho_c] - \frac{\gamma}{2}(\sigma_+\sigma_-\rho_c + \rho_c\sigma_+\sigma_-) = [1/(i\hbar)](H_{\text{eff}}\rho_c - \rho_c H_{\text{eff}}^\dagger), \quad (\text{S.2})$$

in which H_{eff} is a non-Hermitian Hamiltonian. It describes a continuous evolution of the system state with decreasing norm, between randomly occurring spontaneous emission events

$$H_{\text{eff}} = \hbar\Omega(\sigma_+ + \sigma_-) - i\hbar(\gamma/2)\sigma_+\sigma_-. \quad (\text{S.3})$$

The continuous evolution is interrupted by quantum jumps accounted for by the action of the super-operator

$$J\rho_c = \gamma\sigma_-\rho_c\sigma_+. \quad (\text{S.4})$$

The above jump superoperator projects the system state to the ground state ($|\downarrow\rangle$), captures the aftermath of a photon emission. The time τ lapsed (often called waited time) between successive emissions is governed by the waiting-time distribution $w(\tau)$. This exclusive probability density function of the time intervals τ between two consecutive jumps, is given by the expression

$$w(\tau) = \text{Tr}(J e^{\ell\tau}(|\downarrow\rangle\langle\downarrow|)) = \gamma|\langle\uparrow|e^{[1/(i\hbar)]H_{\text{eff}}\tau}|\downarrow\rangle|^2 = \exp\left(-\frac{\gamma\tau}{2}\right)\frac{\gamma\Omega^2}{\mu^2}\sin^2(\mu\tau), \quad (\text{S.5})$$

with $\mu = \frac{1}{2}\sqrt{4\Omega^2 - (\frac{\gamma}{2})^2}$. The waiting-time distribution forms the basis of the quantum-trajectory description of resonance fluorescence in direct photodetection [63], as we will see in the following sections.

3. Dyson expansion and quantum-trajectory formulation in direct photodetection

The solution of the ME (S.1) can be expressed by means of the Dyson expansion [10, 49–51] as follows

$$\rho_c(t) = e^{\ell t}\rho_c(0) + \int_0^t e^{\ell(t-t_1)}J e^{\ell t_1}\rho_c(0) dt_1 + \int_0^t \int_0^{t_2} e^{\ell(t-t_2)}J e^{\ell(t_2-t_1)}J e^{\ell t_1}\rho_c(0) dt_2 dt_1 + \dots \quad (\text{S.6})$$

This form of the solution is very useful to see what an average over all the possible different quantum trajectories is made of, i.e. track the conditioned evolution paths. For example, the first term of the RHS describes a trajectory with no jumps at all. The second term describes all the possible trajectories with one jump at any time instant during the evolution, and so on. In fact, assuming $\rho(0) = |\downarrow\rangle\langle\downarrow|$, this solution can be recast in the explicit form of an average

$$\rho_c(t) = \sum_{n=0}^{\infty} \int_0^t \int_0^{t_n} \dots \int_0^{t_2} dt_n \dots dt_1 \frac{e^{\ell(t-t_n)} (|\downarrow\rangle\langle\downarrow|)}{p_0(t-t_n)} p_n(t, t_1, t_2, \dots, t_n), \quad (\text{S.7})$$

where

$$p_n(t, t_1, t_2, \dots, t_n) = p_0(t-t_n)w(t_n-t_{n-1})\dots w(t_2-t_1)w(t_1) \quad (\text{S.8})$$

is the exclusive probability density for realizing one particular trajectory with n jumps at times t_1, t_2, \dots, t_n and no jumps between t_n and t [5]. Here,

$$p_0(t-t_n) = \text{Tr}(e^{\ell(t-t_n)} |\downarrow\rangle\langle\downarrow|) = e^{-\frac{\gamma(t-t_n)}{2}} \left[\frac{\Omega^2}{\mu^2} - \frac{\gamma^2}{16\mu^2} \cos(2\mu(t-t_n)) + \frac{\gamma}{4\mu} \sin(2\mu(t-t_n)) \right] \quad (\text{S.9})$$

is the null measurement probability density, from the time t_n when the last jump was recorded to the final time t .

a. Ensemble average of nonlinear functions of quantum mechanical expected values

Using the previously derived expressions, one can obtain the following formula for the ensemble average of the quantum mechanical expected value of an operator O :

$$\overline{\langle O(t) \rangle} = \text{Tr}(O\rho_c(t)) = \sum_{n=0}^{\infty} \int_0^t \int_0^{t_n} \dots \int_0^{t_2} dt_n \dots dt_1 \frac{\text{Tr}(Oe^{\ell(t-t_n)} |\downarrow\rangle\langle\downarrow|)}{p_0(t-t_n)} p_n(t, t_1, t_2, \dots, t_n). \quad (\text{S.10})$$

Here, the overbar denotes the ensemble average over all the possible trajectories and the brackets for the quantum mechanical expected value of each one of them. It is the common average obtained from the ME. Based on Eq. (S.10) we can construct a nonlinear average where the single-trajectory quantum mechanical average is raised to some power, i.e., after effecting a nonlinear operation in a post-selection process

$$\overline{\langle O(t) \rangle^m} = \sum_{n=0}^{\infty} \int_0^t \int_0^{t_n} \dots \int_0^{t_2} dt_n \dots dt_1 O_m(t-t_n) w(t_n-t_{n-1}) \dots w(t_2-t_1) w(t_1), \quad (\text{S.11})$$

with

$$O_m(t) = \frac{[\text{Tr}(Oe^{\ell t} (|\downarrow\rangle\langle\downarrow|))]^m}{p_0^{m-1}(t)}, \quad (\text{S.12})$$

a considerably simplified form given that after the last (n) jump the wavefunction has collapsed to $|\downarrow\rangle$ (the individual trajectory is Markovian).

We remark that Eq. (S.11) is an expression which cannot be obtained from the ME without the quantum trajectories point of view of the system evolution. Note that the expression for $\overline{\langle O(t) \rangle^m}$ is just a sum over successive convolutions:

$$\overline{\langle O(t) \rangle^m} = \sum_{n=0}^{\infty} O_m(t-t_n) * \left\{ w(t_n-t_{n-1}) \dots * [w(t_2-t_1) * w(t_1)] \right\}. \quad (\text{S.13})$$

Now, applying the Laplace transform (which we denote as an upper tilde), we obtain the following expression for the ensemble average of the nonlinear quantum mechanical expected value:

$$\widetilde{\overline{\langle O(t) \rangle^m}} = \sum_{n=0}^{\infty} \widetilde{O}_m(z) \widetilde{w}^n(z) = \frac{\widetilde{O}_m(z)}{1 - \widetilde{w}(z)}. \quad (\text{S.14})$$

b. Characteristic examples of nonlinear averages obtained via the Dyson expansion

To illustrate the method, we chose the Pauli operator σ_z and as a nonlinear function of the quantum mechanical average we select the square, i.e., $m = 2$. In this case,

$$\sigma_{z\ m=2}(t) = \frac{[\text{Tr}(\sigma_z e^{\ell t} (|\downarrow\rangle\langle\downarrow|))]^2}{p_0(t)}, \quad (\text{S.15})$$

with the denominator given by Eq. (S.9). Working on the numerator, we obtain the exact expression:

$$\left(\text{Tr}(\sigma_z e^{\ell t} (|\downarrow\rangle\langle\downarrow|))\right)^2 = e^{-\gamma t} \left\{ \frac{1}{2} + \frac{\gamma^2}{32\mu^2} + \frac{1}{2} \left[1 - \frac{\gamma^2}{16\mu^2} \right] \cos(4\mu t) + \frac{\gamma}{4\mu} \sin(4\mu t) \right\}, \quad (\text{S.16})$$

identifying a dominant oscillatory term of frequency 4μ . A frequency mixing, however, is bound to arise due to the denominator $p_0(t)$, albeit scaled by powers of γ/Ω .

The above observation brings us to the strong-driving limit, $Y \gg 1$, with $Y \equiv 2\sqrt{2}\Omega/\gamma$. Neglecting second-order terms in $(\gamma/\Omega)^2 \ll 1$ we write $\mu \approx \Omega$; taking the Laplace transform of $\sigma_{z\ m=2}(t)$, multiplying by $1/[1 - \tilde{w}(z)]$ and going back to the time domain yields the following approximate form:

$$\begin{aligned} \overline{\langle\sigma_z(t)\rangle^2} &\approx \frac{1}{2} + \frac{1}{4} e^{-\frac{3}{4}\gamma t} \left[C_1 \cos(C_\Omega t) + C_2 \sin(C_\Omega t) \right] + \\ &+ \frac{1}{4} e^{-\frac{7}{2}t} \left[C_3 \cos(4\Omega t) + C_4 \sin(4\Omega t) + C_5 \cos(6\Omega t) + C_6 \sin(6\Omega t) \right]. \end{aligned} \quad (\text{S.17})$$

The coefficients C_1, \dots, C_6 depend nonlinearly on the ratio γ/Ω , while $C_\Omega \approx 2\Omega$, in agreement with the occurrence of the pair of eigenvalues with real part $-3\gamma/4$ (distinct from the vertical line at $-\gamma/2$) shown in Fig. S.1.

In the case of σ_y , we find that the form of the solution is the same, and only the coefficients $C_1 - C_6$ change. On the other hand, for the case of σ_x , the solution has an easier form, but it is different from zero only in the presence of a finite detuning Δ between the laser drive and the atomic resonance.

c. Asymptotic results for strong and weak drive in the long-time limit

Let us now consider the long-time limit of the QTAV from the perspective of the final-value theorem in the Laplace Transform. We are still working under $Y \gg 1$ (with $\mu \approx \Omega$). We then obtain

$$\left(\text{Tr}(\sigma_z e^{\ell t} (|\downarrow\rangle\langle\downarrow|))\right)^2 = \frac{1}{2} e^{-\gamma t} [1 + \cos(4\Omega t)] + \mathcal{O}(\gamma/\Omega), \quad (\text{S.18})$$

while $p_0(t) \approx e^{-\gamma t/2} + \mathcal{O}(\gamma/\Omega)$. As we have seen in the previous section, this leaves us to leading order with a damped oscillatory term $e^{-\gamma t/2} \cos^2(2\Omega t) + \mathcal{O}(\gamma/\Omega)$, “screened” by a convolution kernel, the inverse Laplace Transform of $[1 - \tilde{w}(z)]^{-1}$. Applying the final-value theorem, where $[1 - \tilde{w}(z)]^{-1} \approx (z + \gamma/2)/z$ for $z \sim \gamma$, yields $1/2 + \mathcal{O}(\gamma^2/\Omega^2)$ for the long-time limit of $\text{Var}(\sigma_z)$. Given that $S_z \equiv \langle\sigma_z\rangle_{\text{ss}} = 0 + \mathcal{O}(\gamma^2/\Omega^2)$, the asymptotic expression for the time-evolving variance—including first-order terms in γ/Ω of different frequencies—becomes (for $t \gg \gamma^{-1}$)

$$\boxed{\text{Var}(\sigma_z) = \frac{1}{2} \left\{ 1 + e^{-\gamma t/2} \cos(4\Omega t) + \frac{\gamma}{8\Omega} e^{-\gamma t/2} [4 \sin(4\Omega t) - \sin(6\Omega t) - \sin(2\Omega t)] - \frac{\gamma}{4\Omega} e^{-\gamma t/2} \sin(2\Omega t) \right\} + \mathcal{O}(\gamma^2/\Omega^2)}, \quad (\text{S.19})$$

which makes Eq. (3) of the main text, one of our central results. Although limited in its applicability, it shows that all oscillatory terms decay with the same rate, $\gamma/2$, consistent with the eigenvalue distribution plotted in Fig. S.1. Comparing with Eq. (S.17), we expect that the coefficient C_3 does not scale with γ/Ω for $Y \gg 1$ but approaches a constant value. Indeed, we find that $C_3 \approx 2$, while $C_4 \sim 1/Y$. At the same time, the initial-value theorem gives $\text{Var}(\sigma_z)(t \rightarrow 0^+) = 0 + \mathcal{O}(\gamma^2/\Omega^2)$, which we have also numerically confirmed (see Fig. 2 of the main text).

In the opposite limit, $\Omega/\gamma \ll 1$, we use $\mu/\gamma = i\frac{1}{4} + \mathcal{O}((\Omega/\gamma)^2)$. This yields

$$\left(\text{Tr}(\sigma_z e^{\ell t} (|\downarrow\rangle\langle\downarrow|))\right)^2 = e^{-\gamma t} [\cosh(\gamma t) + \sinh(\gamma t)], \quad (\text{S.20})$$

and

$$p_0(t) = e^{-\gamma t/2} [\cosh(\gamma t/2) + \sinh(\gamma t/2)], \quad (\text{S.21})$$

to leading order in Ω/γ . At the same time, from Eq. (S.11) we see that $\tilde{w}(z) \rightarrow 1$ for $z \rightarrow 0$, which means that we cannot use the Laplace transform and the geometric series expansion of $[1 - \tilde{w}(z)]^{-1}$. Instead, we allow at most one jump in the approach to the steady state ($n = 1$) and we directly appeal to the Dyson expansion in the time domain. The asymptotic expression for the variance, then, reads:

$$\boxed{\text{Var}(\sigma_z) = e^{-\gamma t/2} \frac{\cosh \gamma t + \sinh \gamma t}{\cosh(\gamma t/2) + \sinh(\gamma t/2)} - 1 + \mathcal{O}((\Omega/\gamma)^2) = 0 + \mathcal{O}((\Omega/\gamma)^2)}. \quad (\text{S.22})$$

In fact, Monte-Carlo simulations show that $\text{Var}(\sigma_z) \sim 10^{-6}$ for $\gamma/\Omega = 56$.

4. The moment-based method and the truncated hierarchy of equations: Poisson- and Wiener-type unraveling

There are two principal unravelings which define the evolution of the conditioned state vector $|\psi_c\rangle = |\psi_c(t)\rangle$. One is driven by Wiener noise [41, 52] (in this section we set $\hbar = 1$ and denote $\langle A(t) \rangle$ by $\langle A \rangle_t$)

$$\begin{aligned} d|\psi_c\rangle = & -iH|\psi_c\rangle dt + \sum_i \left(\langle L_i^\dagger \rangle_t L_i - \frac{1}{2} L_i^\dagger L_i - \frac{1}{2} |\langle L_i \rangle_t|^2 \right) |\psi_c\rangle dt \\ & + \frac{1}{\sqrt{2}} \sum_i (L_i - \langle L_i \rangle_t) |\psi_c\rangle dW_i(t), \end{aligned} \quad (\text{S.23})$$

where W_i is a complex Wiener process with Itô rule $dW_i^* dW_j = dW_i dW_j^* = 2\delta_{ij} dt$ and all others zero. The other unravelling is driven by Poisson noise [41],

$$\begin{aligned} d|\psi_c\rangle = & - \left(iH + \frac{1}{2} \sum_i L_i^\dagger L_i - \langle L_i^\dagger L_i \rangle_t \right) |\psi_c\rangle dt \\ & + \sum_i \left(\frac{L_i}{\langle L_i^\dagger L_i \rangle_{t-}^{1/2}} - I \right) |\psi_{t-}\rangle dN_i(t), \end{aligned} \quad (\text{S.24})$$

where N_i are real Poisson processes with Itô rule $dN_i dN_j = \delta_{ij} dN_i$ and $dN_i dt = 0$.

We can derive the evolution of the expectation of an observable A by using the Itô product formula [66], $d\langle A \rangle = d\langle \psi_c | A | \psi_c \rangle = (d\langle \psi_c |) A | \psi_c \rangle + \langle \psi_c | A (d|\psi_c\rangle) + (d\langle \psi_c |) A (d|\psi_c\rangle)$. The resulting equations are

$$d\langle A \rangle_t = \langle \mathcal{L}^\dagger[A] \rangle_t dt + \frac{1}{\sqrt{2}} \left[\sum_j \langle A(L_j - \langle L_j \rangle) \rangle_t dW_j(t) + h.c. \right] \quad (\text{S.25})$$

and

$$d\langle A \rangle_t = \langle \mathcal{L}^\dagger[A] \rangle_t dt + \sum_j \left(\frac{\langle L_j^\dagger A L_j \rangle_{t-}}{\langle L_j^\dagger L_j \rangle_{t-}} - \langle A \rangle_{t-} \right) d\tilde{N}_j, \quad (\text{S.26})$$

where $d\tilde{N}_j = dN_j - \langle L_j^\dagger L_j \rangle_t dt$ is the compensated Poisson process (which in the main text assumed the form $d\tilde{N} = dN - \gamma \langle \sigma_+ \sigma_- \rangle_t dt$).

Let us denote by X_i the basis operators of the space of observables, with $x_i = \langle X_i \rangle_t$. In this basis the operators A are described by vectors a , with $a_i = \text{Tr}[A^\dagger X_i]$ so that expectations become inner products $\langle A \rangle_t = (a, x)$. Powers of quantum expectations become powers of inner products and thus if the ensemble average is then taken of these powers, the problem of describing their evolution reduces to finding the evolution of moments, i.e. terms like $\mathbb{E}x_i x_j x_k$. Using equations S.25 and S.26, we can write the evolution equations of x_i as

$$dx_i = (u^i, x) dt + \sum_j f_j^i dW_j + f_j^{i*} dW_j^* \quad (\text{S.27})$$

in the Wiener case with u^i the vector corresponding to $\mathcal{L}^\dagger[X_i]$ and $f_j^i = (f_j^i)_t = \langle X_i(L_j - \langle L_j \rangle)_t \rangle$. In the Poisson case we can similarly write

$$dx_i = (u^i, x)dt + \sum_j g_j^i d\tilde{N}_j, \quad (\text{S.28})$$

with $g_j^i = (g_j^i)_t = \frac{1}{\langle L_j^\dagger L_j \rangle_t} \left(\langle L_j^\dagger X_i L_j \rangle_t - \langle L_j^\dagger L_j \rangle_t \langle X_i \rangle_t \right)$. To calculate the evolution of terms like $\mathbb{E}x_i x_j x_k$, we apply the Itô product formula iteratively to get $d(x_i x_j x_k) = (dx_i)x_j x_k + x_i d(x_j x_k) + dx_i d(x_j x_k)$, then take the expectation so that all martingale terms cancel out. In the Poisson case we use the fact that for a Poisson integral

$$\mathbb{E} \int_0^t f(s) dN_j(s) = \mathbb{E} \int_0^t f(s) \langle L_j^\dagger L_j \rangle_s ds, \quad (\text{S.29})$$

which gives us license to replace $dN_j(t)$ with $\langle L_j^\dagger L_j \rangle_t dt$. Applying these rules leads to very simple combinatorial expressions for the evolution of moments. In the Wiener case, for the second moment we have

$$d\mathbb{E}x_i x_j = \mathbb{E} \left[(u^i, x)x_j + x_i(u^j, x) + \sum_k f_k^{i*} f_k^j + f_k^i f_k^{j*} \right] dt. \quad (\text{S.30})$$

Due to the structure of the Itô product formula, simple combinatorial patterns arise for higher moments:

$$\begin{aligned} d\mathbb{E}x_{i_1} \cdots x_{i_n} &= \mathbb{E} \sum_{j=1}^n (u^{i_j}, x)x_{i_1} \cdots \hat{x}_{i_j} \cdots x_{i_n} dt + \\ &\mathbb{E} \sum_k \sum_{\sigma \in C_2} f_k^{\sigma(i_1)} f_k^{\sigma(i_2)*} x_{\sigma(i_3)} \cdots x_{\sigma(i_n)} dt, \end{aligned} \quad (\text{S.31})$$

where C_k is the set $\{i_1, \dots, i_n\}$ choose k and hat denotes omission. For the Poisson case the pattern is a bit more complex. If l_k denotes the vector representing $L_k^\dagger L_k$, then we have for the quadratic case

$$d\mathbb{E}x_i x_j = \mathbb{E} \left[(u^i, x)x_j + x_i(u^j, x) + \sum_k g_k^i g_k^j (l^k, x) \right] dt \quad (\text{S.32})$$

and for the general case

$$\begin{aligned} d\mathbb{E}x_{i_1} \cdots x_{i_n} &= \mathbb{E} \left[\sum_{j=1}^n (u^{i_j}, x)x_{i_1} \cdots \hat{x}_{i_j} \cdots x_{i_n} + \sum_k \sum_{\sigma \in C_2} g_k^{\sigma(i_1)} g_k^{\sigma(i_2)} x_{\sigma(i_3)} \cdots x_{\sigma(i_n)} (l^k, x) \right. \\ &\left. + \sum_k \sum_{\sigma \in C_3} g_k^{\sigma(i_1)} g_k^{\sigma(i_2)} g_k^{\sigma(i_3)} x_{\sigma(i_4)} \cdots x_{\sigma(i_n)} (l^k, x) + \cdots + \sum_k g_k^{i_1} \cdots g_k^{i_n} (l_k, x) \right] dt, \end{aligned} \quad (\text{S.33})$$

where in this case there is a summation for every set C_l , $l = 1, \dots, n$, each having l many $g_k^{\sigma(i)}$ terms.

In both cases, the evolution is described by a linear equation in the moments (even in the Poisson case where a polynomial division must be performed which has remainder 0), however the equations for the evolution of a moment generally contain higher order moments so the equations do not close. One way to handle this is to truncate at some high order and not consider the evolution of terms beyond that order. Then the system of equations can be solved using standard methods. We can collect the elementary moments $\mathbb{E}x_{i_1} \cdots x_{i_n}$ into a vector y and the coefficients of the moments in each equation $d\mathbb{E}x_{j_1} \cdots x_{j_n}$ to get a matrix, M . This matrix can be exponentiated to arrive at a time evolution for the vector y . To obtain the spectrum of M and the results depicted in Fig. 2 of the main text, a 10th order truncation of the iterative scheme was used. Eigenvalues of the matrix M for $Y = 10, 30$ are plotted in Fig. S.1. They show a banded structure at even multiples of Ω , which gives rise to the characteristic periodicity in the solutions of $\text{Var}(\sigma_z)$. For homodyne and heterodyne detection, closely-spaced eigenvalues of the same imaginary parts give rise to “destructive interference”, dephasing the variance, as we have seen in Fig. 2 of the main text. A similar dephasing is noted in the QTAV $\text{Var}(\sigma_y)$ for direct photodetection, shown in Fig. S.2. Once more, we note the good agreement between the Monte-Carlo simulations, the moment-based method and the Dyson-expansion perturbative treatment to first order in γ/Ω . Evidently, the agreement betters for increasing Y .

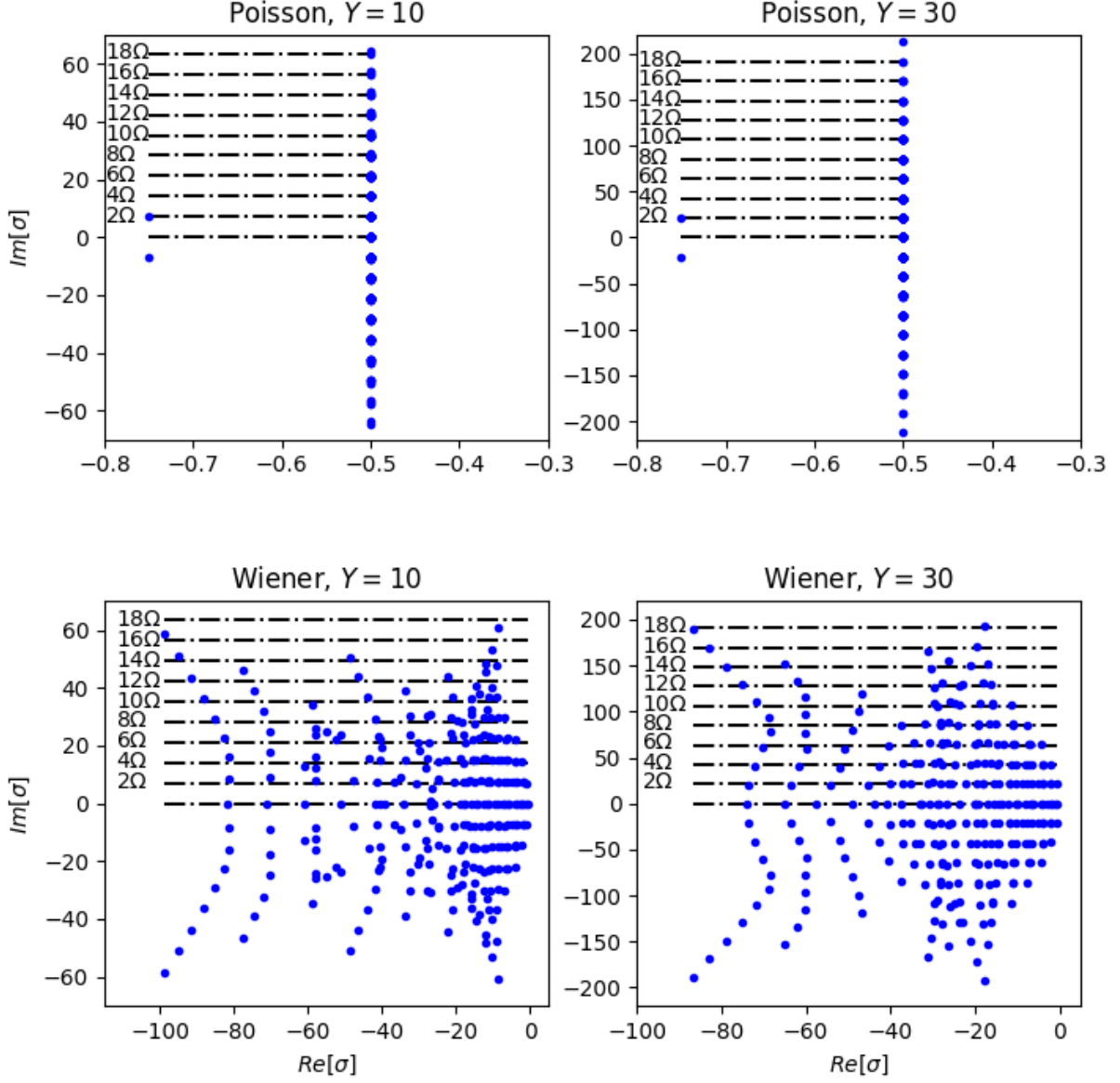


FIG. S.1. Eigenvalues of the dynamical matrix M corresponding to the Poisson and Wiener-type unravelings for $Y = 10, 30$, as indicated on top of each frame. For a Wiener-type unraveling we note that, as Y grows, the spectrum of M aligns better with integer multiples of the Rabi frequency $\Omega_R = 2\Omega$.

5. Direct photoelectron-counting with imperfect detectors and/or a thermal bath

For a limited detector efficiency $\eta < 1$ we cannot use a pure state to describe the evolution between collapses. Instead, the general form must be implemented in density matrix form. Between collapses the propagation rule reads

$$\ell' \rho_c = (\mathcal{L} - \eta J) \rho_c = \frac{1}{i\hbar} [H, \rho_c] + \gamma(1 - \eta) \sigma_- \rho_c \sigma_+ - \frac{\gamma}{2} \{\rho_c, \sigma_+ \sigma_-\}, \quad (\text{S.34})$$

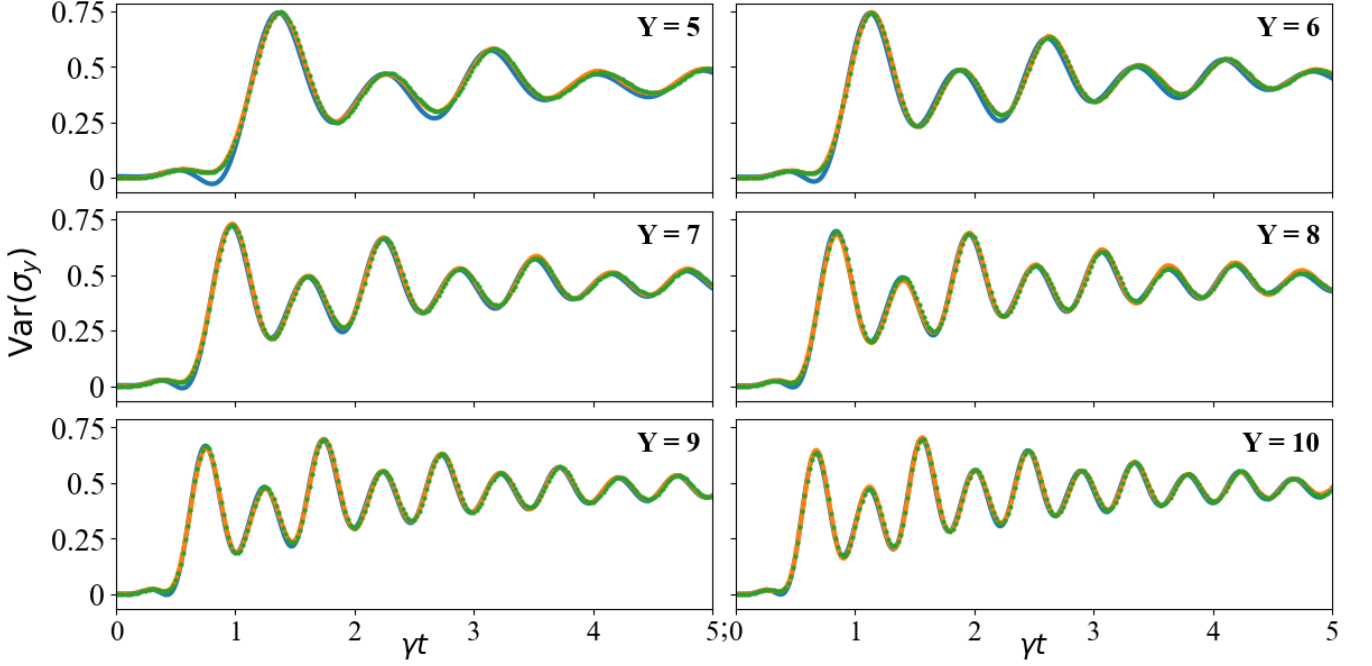


FIG. S.2. Comparison of $\text{Var}(\sigma_y)$ plotted against the dimensionless time γt for the ideal case $\bar{n} = 0$ and $\eta = 1$, with three different methods and for six different driving strengths Y , indicated in the top-right corner of each panel. The Monte-Carlo average over 10^4 realizations is plotted in orange. The blue line and green dots correspond to the analytical results obtained from the Dyson-series expansion to first order in γ/Ω , and the moment-based equations, respectively. As the driving strength increases, so does the agreement between the three methods. Note the negative artefact in the short-time evolution of $\text{Var}(\sigma_y)$, which disappears when higher-order terms in γ^2/Ω^2 are considered in Eq. (S.12). We also remark that in the long-time limit and for $Y \gg 1$, $\text{Var}(\sigma_y) + \text{Var}(\sigma_z) = \frac{1}{2} + \frac{1}{2} = 1$. As in Fig. 2 of the main text, the atom is initialized to its ground state.

($\{.,.\}$ stands for the anti-commutator) while the collapse probability for the interval $(t, t + \Delta t]$ is

$$p_c(t) = \eta \text{tr}[J\rho_c(t)]\Delta t = \eta(\gamma\Delta t)\text{tr}[\rho_c(t)\sigma_+\sigma_-], \quad (\text{S.35})$$

and the (un-normalized) state becomes $\eta J\rho_c$. For $\eta \ll 1$, a single trajectory closely follows the deterministic evolution governed by the ME. This explains the significant reduction in the variance (the case for very weak drive), which – as we have seen in the main text – “responds” to quantum jumps and the oscillatory regression of the fluctuation.

If we now admit a thermal light injecting a photon flux $\gamma\bar{n}$, then the following term is added to the coherent evolution between collapses [to RHS of Eq. (S.34)]:

$$\gamma\bar{n}(\sigma_-\rho_c\sigma_+ + \sigma_+\rho_c\sigma_- - \sigma_+\sigma_-\rho_c - \rho_c\sigma_-\sigma_+). \quad (\text{S.36})$$

In the ideal case, $\bar{n} = 0$, $\eta = 1$, the series of photon “clicks” fully defines the quantum trajectory, since the wavefunction evolves under the action of H_{eff} defined in Eq. (S.3), being reset to the ground state after a spontaneous emission occurs. At optical frequencies, one has $\bar{n} \ll 1$, whence the most detrimental factor to the coherence of individual realizations is the limited detector efficiency. In that case, the propagation rule of Eq. (S.34) must be used between jumps which, for $\eta \ll 1$, coincides with the action of the Lindblad superoperator \mathcal{L} . Photoelectron counting and waiting-time distributions for nonunit detection efficiency are presented in [63].

6. Homodyne detection and quadrature amplitude squeezing

Let us briefly discuss a third type of unravelling (one of Wiener type), in addition to direct photodetection and heterodyne detection, the latter being equivalent to the quantum-state diffusion model [52]. In 1981, Walls and Zoller [64] reported that light scattered in resonance fluorescence is squeezed in the field quadrature that is in phase with the mean scattered field amplitude, proportional to $\langle\sigma_-\rangle_{\text{ss}} = +iY/(1+Y^2)$ in the steady state, whence in a direction along $\theta = \pi/2$. A year later, Mandel came up with a scheme for detecting squeezing, which involved

homodyning the scattered light with a strong local oscillator and measuring photon counting statistics as a function of the local oscillator phase [65]. Following this approach, the (un-normalized) conditional wavefunction evolves according to the stochastic Schrödinger equation

$$\frac{d}{dt} |\bar{\psi}_c\rangle = \frac{1}{i\hbar} H_W(t) |\bar{\psi}_c\rangle, \quad (\text{S.37})$$

in which $H_W(t)$ is the stochastic non-Hermitian Hamiltonian:

$$H_W(t) = H - i\hbar\gamma\sigma_+\sigma_- + i\hbar[\sqrt{\gamma}\langle\psi_c(t)|e^{i\theta}\sigma_+ + e^{-i\theta}\sigma_-\rangle|\psi_c(t)\rangle + \eta_W(t)]e^{-i\theta}\sqrt{\gamma}\sigma_-, \quad (\text{S.38})$$

where θ is the local-oscillator phase, $|\psi_c(t)\rangle$ is the normalized state and η_W is a Gaussian white noise. Instances of the conditional variance $\text{Var}(\sigma_z)$ under this unravelling are depicted in Fig. 2 of the main text for $\theta = \pi/2$ and $\theta = 0$. For an imperfect detector, the noise η_W is replaced by two uncorrelated noise sources added in the proportion η and $1 - \eta$, with the former featuring in the photocurrent while the latter not [10]. In Fig. 2 of the main text (bottom panels) we show that the QTAV $\text{Var}(\sigma_z)$ captures the redistribution of fluctuations among the squeezed and anti-squeezed quadratures. Finally, we recall that in heterodyne detection, θ is effectively replaced by $-(\omega_{LO} - \omega_A)t$ (see Fig. 1 of the main text). The frequency mismatch between the local oscillator and the drive (here resonant with the atom) is assumed to be very large in comparison to the field fluctuations ($\sim \gamma$). A time average over the period $2\pi/(\omega_{LO} - \omega_A)$ is then performed to simplify the resulting stochastic Schrödinger equation.

7. EPR steering for system-environment entanglement

We will now digress a little to discuss the relevance of the QTAV and its evolution vis-a-vis the discussion of Wiseman and Gambetta in Ref. [70] on EPR steering for resonance fluorescence with $Y \gg 1$. In such a configuration, Bob has direct access to the coherently driven two-state system while Alice is situated in the environment where she is able to alternate between unravelings. Then the objective quantum state assumption entails the inequality [69]

$$S(\rho^{c,D}, \rho^{c,H}) \equiv \overline{f_1(\rho^{c,D})} + \overline{f_2(\rho^{c,H})} \leq 1, \quad (\text{S.39})$$

where $f_1(\rho) \equiv (\text{tr}[\sigma_x\rho])^2$ and $f_2(\rho) \equiv (\text{tr}[\sigma_y\rho])^2 + (\text{tr}[\sigma_z\rho])^2$; here ρ a state conditioned on a particular measurement scheme selected by Alice.

In assessing whether the EPR steering inequality can be violated in our case, the superscripts D and H denote direct photodetection in vacuum ($\bar{n} = 0$) and heterodyne detection, respectively (the latter performed with unit efficiency). Therefore, $\rho^{c,D}$ solves ME (1) with $\ell \rightarrow \ell'$ from Eq. (S.34), yielding a mixed state, while $\rho^{c,H}$ solves Eq. (S.23) yielding a pure state at all times.

Figure S.3 plots the value of S for different values of Y and η . As noted in [70], for $S > 1$ the experiment would rule out all theories of objective atomic state reduction. For unit-efficiency direct detection ($\eta = 1$), the steady-state value of S always exceeds unity. We note the envelope is primarily determined by the detection efficiency while the carrier frequency is set by Y . Figures S.3(c, d) show that the envelope drops below unity for $\eta \lesssim 0.8$, satisfying the inequality (S.39), whence making the experiment “not provably measurement dependent”. In contrast, we note that the feedback scheme adopted for direct photodetection in [70] guarantees $S > 1$ for any value of η and a perfect heterodyne detector.

8. Experimental setup and considerations

In this section, we describe the different experimental imperfections that can affect the measurements of a linear average of σ_z : the second-order correlation $g^{(2)}(\tau)$. The same spirit could be applied for non-linear averages. Second-order correlation functions are routinely measured experimentally using photon counting techniques in a Hanbury Brown and Twiss configuration. The photon flux enters a beam-splitter and both outputs are monitored by two detectors after a long integration time.

We consider real experimental data based on the setup of [57] in order to highlight the different imperfections. The experimental setup consists of a Maltese-cross coupling of single neutral atoms of ^{87}Rb . The atom is illuminated by a laser field with Rabi frequency Ω and detuning Δ . The photons are collected by high-numerical aperture lenses, as shown in the main text, and the photon arrival times are measured [Fig. S.4(a)] using single-photon avalanche photodiodes (APDs). From these measurements, the normalized second-order correlation function between the lenses L1 and L2 is computed [Fig. S.4(b)]. The average atomic scattering rate on a single detector is $R_{\text{sca,det}} = 9000$ counts/s.

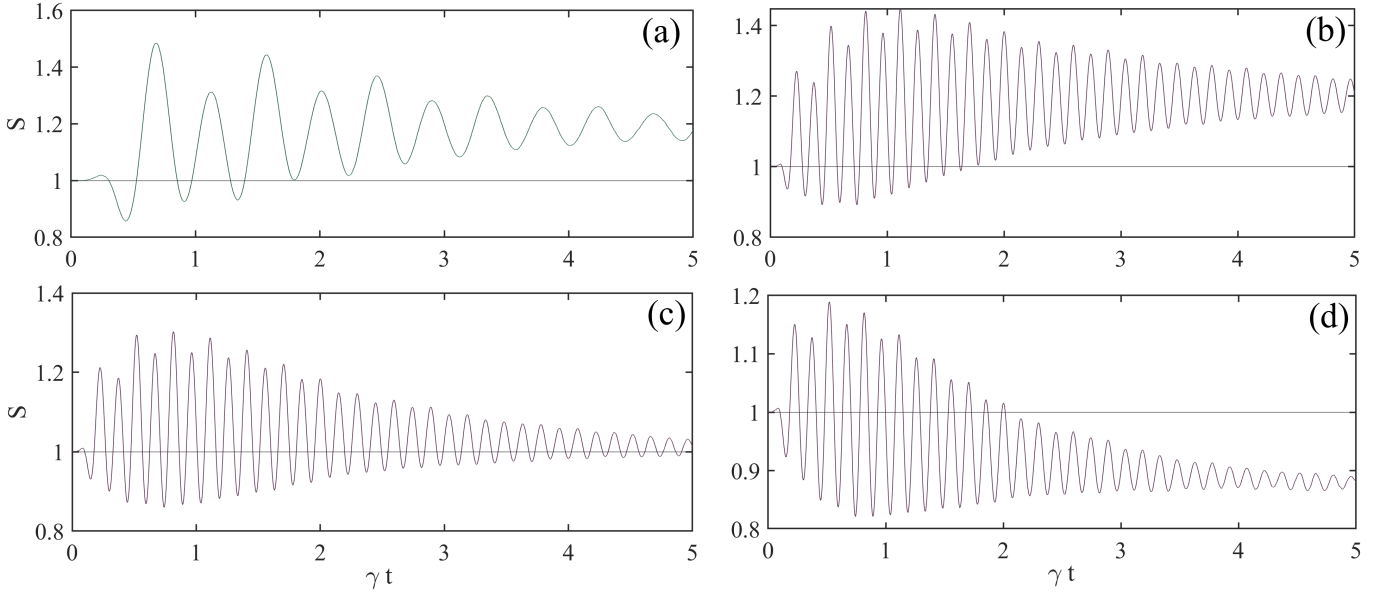


FIG. S.3. EPR steering $S = S(\rho^{c,D}, \rho^{c,H})$ value from the inequality (S.39) for: $Y = 10$ and $\eta = 1$ in (a), $Y = 30$ and $\eta = 1$ in (b), $Y = 30$ and $\eta = 0.8$ in (c), and $Y = 30$ and $\eta = 0.6$ in (d).

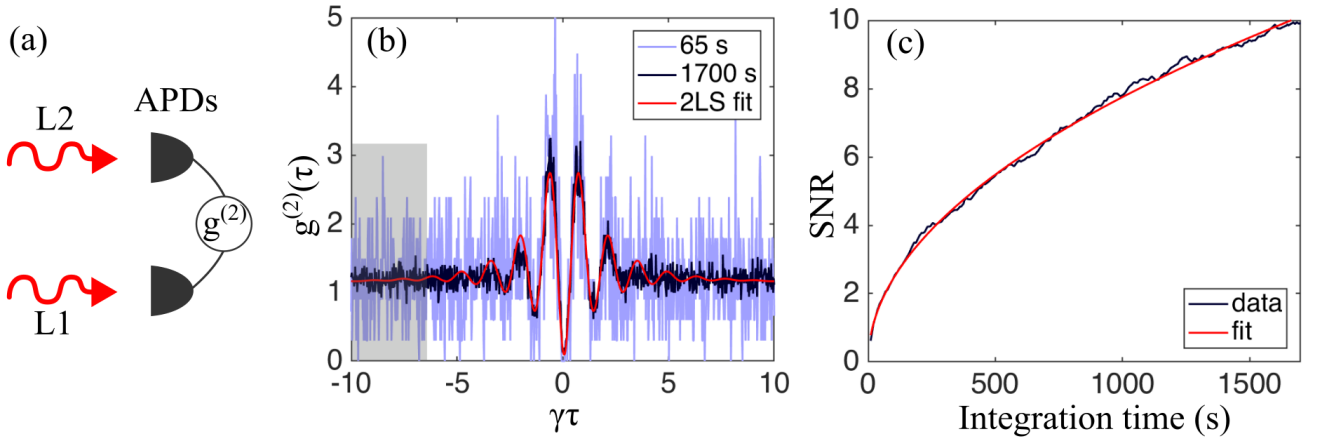


FIG. S.4. (a) The arrival times of the photons coming from the lenses L1 and L2 are measured by avalanche photodiodes (APDs). (b) Normalized second-order correlation function for integration times of 65 (blue) or 1700 (black) seconds and fit using Eq. (S.40) from a two-level system approximation including experimental imperfections (red). The gray shaded box corresponds to the time range where the signal-to noise of $g^{(2)}$ is computed and shown in (c) as a function of the integration time and fitted by Eq. (S.41).

Let us focus on the measured correlation $g_{\text{mes}}^{(2)}(\tau)$ after a long integration time. The fit function for the correlation based on a two-level atom model and including different experimental imperfections is given by:

$$g_{\text{mes}}^{(2)}(\tau) = \frac{A(\tau)g^{(2)}(\tau, \Delta, \Omega) + \frac{2}{\text{SNR}_{\text{Det}}} + \frac{1}{\text{SNR}_{\text{Det}}^2}}{1 + \frac{2}{\text{SNR}_{\text{Det}}} + \frac{1}{\text{SNR}_{\text{Det}}^2}}, \quad (\text{S.40})$$

where $\text{SNR}_{\text{Det}} = R_{\text{sca,det}}/R_{\text{DC}} = 18$ accounts for false positive photon detections due to the dark counts of the detectors. In the experiment, the dark count rate was $R_{\text{DC}} = 500$ counts/s for each detector. Then, for single atoms, the photon counts are usually measured using red-detuned light in order to maintain the atom in the trap while acquiring the resonance fluorescence signal. A large negative detuning $\Delta < 0$ causes an overshoot of the maximum value of $g^{(2)}$ above 2. It is taken into account by an explicit dependence on the detuning of $g^{(2)}(\tau, \Delta, \Omega)$ which comes from the steady-state solution of the optical Bloch equations for a two-level atom. Finally, an empirical global envelop

$A(\tau) = a + be^{-c\tau}$ takes into account the effect of the atomic motion in the trap [58] where the parameters a, b, c are extracted from a fit on microsecond timescales. After including these corrections, the correlation function is fitted from which we extract the Rabi frequency $\Omega = 3.3\gamma$ and the detuning $\Delta = -3.2\gamma$. As shown on Fig. S.4(c), modeling the atom as a two-level system including experimental imperfections is enough to explain the experimental data. This agreement justifies the use of a two-level atom model to compute the different unravelings.

Now, let us consider that each photon flux arriving on the two detectors is measured with same efficiency η . In an optical detection system, η is given by the product of the collection efficiency η_{col} , the optical path losses η_{loss} and the quantum efficiency of the detectors η_{QE} . The $g^{(2)}$ statistics is recovered by measuring coincidences on two detectors over a large dataset after a long integration time t_{int} . In the long time limit ($\gamma\tau \gg 1$), where the counts are uncorrelated, the coincidences follow a Poissonian statistics. Therefore, the signal-to-noise SNR of the measured $g^{(2)}$ scales as:

$$\text{SNR} = \sqrt{\eta^2 g^{(2)} R_{\text{sca,det}} t_{\text{int}}}. \quad (\text{S.41})$$

Experimentally, we evaluate the signal-to-noise of the measured $g_{\text{mes}}^{(2)}$ [Fig. S.4(c)] by computing the ratio of the average and the standard deviation in the steady-state limit [gray shaded area in Fig. S.4(b)].

By fitting the signal-to-noise using Eq. (S.41), we end up with $\eta = 0.25\%$. First, the optical losses $\eta_{\text{loss}} = 50\%$ can be improved by a better mode-matching of the emitting spatial modes and the collecting optical fibers. Second, the detector quantum efficiency $\eta_{\text{QE}} = 50\%$ at a specific wavelength $\lambda = 780$ nm can be increased up to 90% using superconducting nanowires [67]. Finally, for an atom scattering photons isotropically, the collection efficiency η_{col} is determined by the solid angle covered by the optical system. Based on these numbers, we deduce the experimental collection efficiency of a single lens of 1%. By summing all channels up, the Maltese-cross coupling scheme employing the four lenses increases in principle this coupling by a factor of 4 for an atom tightly trapped in all spatial directions. Other geometries could also be used to increase the collection efficiency, such as a parabolic mirror trap [68].

ACKNOWLEDGMENTS

We gratefully acknowledge funding from: ERC AdG NOQIA; MCIN/AEI (PGC2018-0910.13039/501100011033, CEX2019-000910-S/10.13039/501100011033, Plan National FIDEUA PID2019-106901GB-I00, Plan National STAMEENA PID2022-139099NB-I00 project funded by MCIN/AEI/10.13039/501100011033 and by the “European Union NextGenerationEU/PRTR” (PRTR-C17.I1), FPI); QUANTERA MAQS PCI2019-111828-2); QUANTERA DYNAMITE PCI2022-132919 (QuantERA II Programme co-funded by European Union’s Horizon 2020 program under Grant Agreement No 101017733), Ministry of Economic Affairs and Digital Transformation of the Spanish Government through the QUANTUM ENIA project call – Quantum Spain project, and by the European Union through the Recovery, Transformation, and Resilience Plan – NextGenerationEU within the framework of the Digital Spain 2026 Agenda; Fundació Cellex; Fundació Mir-Puig; Generalitat de Catalunya (European Social Fund FEDER and CERCA program, AGAUR Grant No. 2021 SGR 01452, QuantumCAT/U16-011424, co-funded by ERDF Operational Program of Catalonia 2014-2020); Barcelona Supercomputing Center MareNostrum (FI-2023-1-0013); EU Quantum Flagship (PASQuanS2.1, 101113690); EU Horizon 2020 FET-OPEN OPTologic (Grant No 899794); EU Horizon Europe Program (Grant Agreement 101080086 — NeQST), ICFO Internal “QuantumGaudi” project; European Union’s Horizon

2020 program under the Marie Skłodowska-Curie grant agreement No 847648; “La Caixa” Junior Leaders fellowships, La Caixa” Foundation (ID 100010434): CF/BQ/PR23/11980043, LCF/BQ/PR23/11980044; European Commission project QUANTIFY (Grant Agreement No. 101135931); Spanish Ministry of Science MCIN: project SAPONARIA (PID2021-123813NB-I00) and “Severo Ochoa” Center of Excellence CEX2019-000910-S; Departament de Recerca i Universitats de la Generalitat de Catalunya grant No. 2021 SGR 01453. Views and opinions expressed are, however, those of the author(s) only and do not necessarily reflect those of the European Union, European Commission, European Climate, Infrastructure and Environment Executive Agency (CINEA), or any other granting authority. Neither the European Union nor any granting authority can be held responsible for them. MAG-M acknowledges funding from QuantERA II Cofund 2021 PCI2022-133004, Projects of MCIN with funding from European Union NextGenerationEU (PRTR-C17.I1) and by Generalitat Valenciana, with Ref. 20220883 (PerovsQuTe) and COMCUANTICA/007 (QuantTwin), and Red Tematica RED2022-134391-T. JW was partially supported by NSF grant DMS 1911358 and by the Simons Foundation Fellowship 823539.

- [1] V. Gorini, A. Kossakowski, and E. C. G. Sudarshan, *Journal of Mathematical Physics* **17**, 821 (1976).
- [2] G. Lindblad, *Communications in Mathematical Physics* **48**, 119 (1976).
- [3] H.-P. Breuer and F. Petruccione, in *Open Systems and Measurement in Relativistic Quantum Theory*, edited by H.-P. Breuer and F. Petruccione (Springer Berlin Heidelberg, Berlin, Heidelberg, 1999) pp. 81–116.
- [4] S. Haroche and J.-M. Raimond, *Exploring the Quantum: Atoms, Cavities, and Photons* (Oxford University Press, 2006).
- [5] H. P. Breuer and F. Petruccione, *The theory of open quantum systems* (Oxford university press, 2002).
- [6] S. Attal, A. Joye, and C.-A. Pillet, eds., *Open Quantum Systems II – The Markovian Approach*, Vol. 1881 (Springer Berlin, Heidelberg, 2006) lecture Notes in Mathematics.
- [7] H. Carmichael, *Statistical Methods in Quantum Optics 2* (Springer, Berlin, Germany, 2008) Chap. 9, 17.
- [8] L. Accardi, I. Volovich, and Y. G. Lu, *Quantum Theory and Its Stochastic Limit* (Springer Berlin, Heidelberg, 2013).
- [9] H. K. N. Bohr and J. Slater, *The London, Edinburgh, and Dublin Philosophical Magazine and Journal of Science* **47**, 785 (1924).
- [10] H. Carmichael, *An open systems approach to quantum optics* (Springer, Berlin, Germany, 1993).
- [11] C. W. Gardiner, A. S. Parkins, and P. Zoller, *Phys. Rev. A* **46**, 4363 (1992).
- [12] J. Dalibard, Y. Castin, and K. Mølmer, *Phys. Rev. Lett.* **68**, 580 (1992).
- [13] R. Omnès, *The Interpretation of Quantum Mechanics* (Princeton University Press, Princeton, New Jersey, 1994).
- [14] P. Blanchard and A. Jadczyk, *Annalen der Physik* **507**, 583 (1995).
- [15] A. N. Korotkov, *Phys. Rev. B* **60**, 5737 (1999).
- [16] M. B. Plenio and P. L. Knight, *Rev. Mod. Phys.* **70**, 101 (1998).
- [17] G. C. Hegerfeldt and D. G. Sondermann, *Quantum and Semiclassical Optics: Journal of the European Optical Society Part B* **8**, 121 (1996).
- [18] A. J. Daley, *Advances in Physics* **63**, 77 (2014).
- [19] D. J. Wineland and H. Dehmelt, *Bull. Am. Phys. Soc.* **20**, 637 (1975).
- [20] H. Dehmelt, *J. Phys. Colloques* **42**, C8 (1981).
- [21] W. Nagourney, J. Sandberg, and H. Dehmelt, *Phys. Rev. Lett.* **56**, 2797 (1986).
- [22] T. Sauter, W. Neuhauser, R. Blatt, and P. E. Toschek, *Phys. Rev. Lett.* **57**, 1696 (1986).
- [23] J. C. Bergquist, R. G. Hulet, W. M. Itano, and D. J. Wineland, *Phys. Rev. Lett.* **57**, 1699 (1986).
- [24] T. Basché, S. Kummer, and C. Bräuchle, *Nature* **373**, 132 (1995).
- [25] S. Peil and G. Gabrielse, *Phys. Rev. Lett.* **83**, 1287 (1999).
- [26] S. Gleyzes, S. Kuhr, C. Guerlin, J. Bernu, S. Deléglise, U. Busk Hoff, M. Brune, J.-M. Raimond, and S. Haroche, *Nature* **446**, 297 (2007).
- [27] P. Neumann, J. Beck, M. Steiner, F. Rempp, H. Fedder, P. R. Hemmer, J. Wrachtrup, and F. Jelezko, *Science* **329**, 542 (2010).
- [28] R. Vijay, D. H. Slichter, and I. Siddiqi, *Phys. Rev. Lett.* **106**, 110502 (2011).
- [29] Z. K. Mineev, S. O. Mundhada, S. Shankar, P. Reinhold, R. Gutiérrez-Jáuregui, R. J. Schoelkopf, M. Mirrahimi, H. J. Carmichael, and M. H. Devoret, *Nature* **570**, 200 (2019).
- [30] R. J. Cook and H. J. Kimble, *Phys. Rev. Lett.* **54**, 1023 (1985).
- [31] H. J. Kimble, R. J. Cook, and A. L. Wells, *Phys. Rev. A* **34**, 3190 (1986).
- [32] T. Erber and S. Putterman, *Nature* **318**, 41 (1985).
- [33] J. Javanainen, *Phys. Rev. A* **33**, 2121 (1986).
- [34] A. Schenzle, R. G. DeVoe, and R. G. Brewer, *Phys. Rev. A* **25**, 2606 (1982).
- [35] C. Cohen-Tannoudji and J. Dalibard, *Europhysics Letters* **1**, 441 (1986).
- [36] R. J. Cook, *Physica Scripta* **1988**, 49 (1988).
- [37] G. C. Hegerfeldt and M. B. Plenio, *Phys. Rev. A* **46**, 373 (1992).
- [38] G. C. Hegerfeldt and M. B. Plenio, *Phys. Rev. A* **47**, 2186 (1993).
- [39] G. C. Hegerfeldt, “The quantum jump approach and some of its applications,” in *Time in Quantum Mechanics - Vol. 2*, edited by G. Muga, A. Ruschhaupt, and A. del Campo (Springer Berlin Heidelberg, Berlin, Heidelberg, 2009) pp. 127–174.
- [40] D. Keys and J. Wehr, *Journal of Mathematical Physics* **61**, 032101 (2020).
- [41] A. Barchielli and V. P. Belavkin, *Journal of Physics A: Mathematical and General* **24**, 1495 (1991).
- [42] T. A. Brun, *American Journal of Physics* **70**, 719 (2002).
- [43] A. Barchielli, “Continual measurements in quantum mechanics and quantum stochastic calculus,” in *Open Quantum Systems III: Recent Developments*, edited by S. Attal, A. Joye, and C.-A. Pillet (Springer Berlin Heidelberg, Berlin, Heidelberg, 2006) pp. 207–292.
- [44] V. P. Belavkin, *Letters in Mathematical Physics* **20**, 85 (1990).
- [45] V. Belavkin and P. Staszewski, *Reports on Mathematical Physics* **29**, 213 (1991).
- [46] G. C. Ghirardi, P. Pearle, and A. Rimini, *Phys. Rev. A* **42**, 78 (1990).
- [47] G. C. Ghirardi, A. Rimini, and T. Weber, *Phys. Rev. D* **34**, 470 (1986).
- [48] E. Davies, *Quantum Theory of Open Systems* (Academic Press, 1976).
- [49] M. D. Srinivas and E. B. Davies, *Optica Acta: International Journal of Optics* **28**, 981 (1981).
- [50] P. Zoller, M. Marte, and D. F. Walls, *Phys. Rev. A* **35**, 198 (1987).
- [51] R. Dum, P. Zoller, and H. Ritsch, *Phys. Rev. A* **45**, 4879 (1992).
- [52] N. Gisin and I. C. Percival, *Journal of Physics A: Mathematical and General* **25**, 5677 (1992).
- [53] H. J. Carmichael, in *Quantum Future From Volta and Como to the Present and Beyond*, edited by P. Blanchard and A. Jadczyk (Springer Berlin Heidelberg, Berlin, Heidelberg, 1999) pp. 15–36.
- [54] R. Durrett, *Probability: Theory and Examples*, 5th ed., Cambridge Series in Statistical and Probabilistic Mathe-

- matics (Cambridge University Press, 2019).
- [55] H. M. Wiseman and G. J. Milburn, *Phys. Rev. A* **47**, 642 (1993).
- [56] H. Nha and H. J. Carmichael, *Phys. Rev. Lett.* **93**, 120408 (2004).
- [57] N. Bruno, L. C. Bianchet, V. Prakash, N. Li, N. Alves, and M. W. Mitchell, *Opt. Express* **27**, 31042 (2019).
- [58] M. Weber, J. Volz, K. Saucke, C. Kurtsiefer, and H. Weinfurter, *Phys. Rev. A* **73**, 043406 (2006).
- [59] see Supplementary Material.
- [60] B. R. Mollow, *Phys. Rev. A* **12**, 1919 (1975).
- [61] R. J. Cook, *Optics Communications* **35**, 347 (1980).
- [62] R. J. Cook, *Phys. Rev. A* **23**, 1243 (1981).
- [63] H. J. Carmichael, S. Singh, R. Vyas, and P. R. Rice, *Phys. Rev. A* **39**, 1200 (1989).
- [64] D. F. Walls and P. Zoller, *Phys. Rev. Lett.* **47**, 709 (1981).
- [65] L. Mandel, *Phys. Rev. Lett.* **49**, 136 (1982).
- [66] D. M. Keys, “A quantum stochastic approach to poisson master equation unravellings and ghirardi-rimini-weber theory,” (2022).
- [67] C. M. Natarajan, M. G. Tanner, and R. H. Hadfield, *Superconductor Science and Technology* **25**, 063001 (2012).
- [68] C.-K. Chou, C. Aucher, J. Lilieholm, K. Smith, and B. Blinov, *Review of Scientific Instruments* **88**, 086101 (2017).
- [69] S. J. Jones, H. M. Wiseman, and A. C. Doherty, *Phys. Rev. A* **76**, 052116 (2007).
- [70] H. M. Wiseman and J. M. Gambetta, *Phys. Rev. Lett.* **108**, 220402 (2012).
- [71] S. Daryanoosh and H. M. Wiseman, *New Journal of Physics* **16**, 063028 (2014).
- [72] A. Barchielli and M. Gregoratti, *Philosophical Transactions of the Royal Society A: Mathematical, Physical and Engineering Sciences* **370**, 5364 (2012).
- [73] S. Arranz Regidor, G. Crowder, H. Carmichael, and S. Hughes, *Phys. Rev. Res.* **3**, 023030 (2021).
- [74] J. Preskill, *Quantum* **2**, 79 (2018).
- [75] E. Altman, K. R. Brown, G. Carleo, L. D. Carr, E. Demler, C. Chin, B. DeMarco, S. E. Economou, M. A. Eriksson, K.-M. C. Fu, M. Greiner, K. R. Hazzard, R. G. Hulet, A. J. Kollár, B. L. Lev, M. D. Lukin, R. Ma, X. Mi, S. Misra, C. Monroe, K. Murch, Z. Nazario, K.-K. Ni, A. C. Potter, P. Roushan, M. Saffman, M. Schleier-Smith, I. Siddiqi, R. Simmonds, M. Singh, I. Spielman, K. Temme, D. S. Weiss, J. Vučković, V. Vuletić, J. Ye, and M. Zwierlein, *PRX Quantum* **2**, 017003 (2021).
- [76] J. Fraxanet, T. Salamon, and M. Lewenstein, “The coming decades of quantum simulation,” (2022), arXiv:2204.08905 [quant-ph].
- [77] B. Skinner, J. Ruhman, and A. Nahum, *Phys. Rev. X* **9**, 031009 (2019).
- [78] Y. Li, X. Chen, and M. P. A. Fisher, *Phys. Rev. B* **98**, 205136 (2018).
- [79] Y. Li, X. Chen, and M. P. A. Fisher, *Phys. Rev. B* **100**, 134306 (2019).
- [80] A. Chan, R. M. Nandkishore, M. Pretko, and G. Smith, *Phys. Rev. B* **99**, 224307 (2019).
- [81] P. Sierant and X. Turkeshi, *Phys. Rev. Lett.* **128**, 130605 (2022).
- [82] X. Turkeshi, R. Fazio, and M. Dalmonte, *Phys. Rev. B* **102**, 014315 (2020).
- [83] O. Lunt, M. Szyniszewski, and A. Pal, *Phys. Rev. B* **104**, 155111 (2021).
- [84] P. Sierant, M. Schirò, M. Lewenstein, and X. Turkeshi, *Phys. Rev. B* **106**, 214316 (2022).
- [85] X. Cao, A. Tilloy, and A. D. Luca, *SciPost Phys.* **7**, 024 (2019).
- [86] G. Piccitto, A. Russomanno, and D. Rossini, *Phys. Rev. B* **105**, 064305 (2022).
- [87] M. Kolodrubetz, *Phys. Rev. B* **107**, L140301 (2023).
- [88] X. Turkeshi, A. Biella, R. Fazio, M. Dalmonte, and M. Schiró, *Phys. Rev. B* **103**, 224210 (2021).
- [89] P. Sierant and X. Turkeshi, *Phys. Rev. Lett.* **130**, 120402 (2023).
- [90] M. Buchhold, T. Müller, and S. Diehl, arXiv:2208.10506.
- [91] T. Iadecola, S. Ganeshan, J. H. Pixley, and J. H. Wilson, *Phys. Rev. Lett.* **131**, 060403 (2023).
- [92] L. Piroli, Y. Li, R. Vasseur, and A. Nahum, *Phys. Rev. B* **107**, 224303 (2023).
- [93] N. O’Dea, A. Morningstar, S. Gopalakrishnan, and V. Khemani, arXiv:2211.12526.
- [94] V. Ravindranath, Y. Han, Z.-C. Yang, and X. Chen, *Phys. Rev. B* **108**, L041103 (2023).
- [95] V. Ravindranath, Z.-C. Yang, and X. Chen, “Free fermions under adaptive quantum dynamics,” (2023), arXiv:2306.16595 [quant-ph].
- [96] P. Sierant and X. Turkeshi, “Entanglement and absorbing state transitions in $(d + 1)$ -dimensional stabilizer circuits,” (2023), arXiv:2308.13384 [cond-mat.stat-mech].